Details of pearlite to austenite transformation in steel
Experiments and phase-field modeling

Mattos Ferreira, V.; Mecozzi, M. G.; Petrov, R. H.; Sietsma, J.

DOI
10.1016/j.commatsci.2023.112368

Publication date
2023

Document Version
Final published version

Published in
Computational Materials Science

Computational Materials Science 228 (2023) 112368

Contents lists available at ScienceDirect

Computational Materials Science

journal homepage: www.elsevier.com/locate/commatsci

Full length article

Details of pearlite to austenite transformation in steel: Experiments and phase-field modeling

V. Mattos Ferreira [a,*], M.G. Mecozzi [a], R.H. Petrov [a,b], J. Sietsma [a]

[a] Delft University of Technology, Department of Materials Science and Engineering, Mekelweg 2, 2628 CD Delft, The Netherlands
[b] Ghent University, Department of Electrical Energy, Metals, Mechanical Constructions and Systems, Technologiepark 903, Ghent, Belgium

ARTICLE INFO

Keywords:
Phase-field modeling
Phase transformation
Pearlite

ABSTRACT

The austenitization of an initial pearlitic microstructure is simulated using the phase field model to achieve insight into White Etching Layer (WEL) formation in pearlitic railway steels. The simulations take into account the resolution of the cementite lamellae within a pearlite colony as well as the presence of pro-eutectoid ferrite. The austenite growth kinetics and morphology obtained via simulations are compared with dilatometry and microscopy observations. The influence of γ/θ and γ/α mobilities on the austenite growth morphology are studied. The simulations reproduce the microstructural features as well as the experimentally observed kinetics behavior of austenite formation, involving the correlation between mobilities and nucleation behavior.

1. Introduction

Railway steels are subjected to complex loading conditions during service due to wheel and rail contact leading to the development of rolling contact fatigue (RCF), the dominant damage mechanism in rails [1]. Several studies have identified the microstructural aspects of RCF damage development in railway steels, such as inclusions, pro-eutectoid ferrite, and microstructural changes in the rail's surface, known as White Etching Layers (WEL) [2–5]. WEL develops due to wheel and rail contacts and is detrimental to rail service life as it is associated with preferential sites for crack nucleation and growth due to its brittle nature [6,7]. For this reason, it is critical to comprehend the mechanisms that occur during WEL formation in order to design appropriate methods of reducing or preventing its occurrence.

In the past years, the microstructural features of different WEL found in railway steel grades have been extensively investigated. As a result, several hypotheses were developed to explain the mechanisms of WEL development [8–10]. One of these hypotheses argues that WEL is formed due to temperature rise during wheel and rail contact [11–13]. Basically, the wheel and rail contact would generate sufficient heat to increase the temperature at the rail surface above austenitization temperatures. The austenite would then be transformed into martensite during fast cooling, forming the WEL.

However, it is not possible to exactly determine the temperature profile and mechanical loading during heating of the railway surface due to the small contact area and very short time scale. This leads to difficulties when trying to reproduce the field conditions in a laboratory setup. Even if the temperature profile would be known, the characterization of austenite (γ), which is stable at high temperatures, is quite complex. Therefore, the understanding of austenite formation in such conditions remains a challenge.

Some studies have experimentally investigated the microstructural features of austenite formation in pearlite. Speich et al. [14] separated the kinetics of austenite formation in dual-phase steels into three stages. First, the nucleation of austenite at ferrite/pearlite interfaces with rapid growth of austenite into pearlite as it is controlled by C diffusion over very short diffusion distances. The growth rate is then greatly reduced when austenite grows into pro-eutectoid ferrite. The final step would be the Mn equilibration in austenite which is a very long process. Shtansky et al. [15] focused on the morphology of nucleation and growth of austenite from pearlite using Transmission Electron Microscopy (TEM). Nucleation of austenite seemed to occur preferentially at the pearlite colony boundaries. However, some nuclei were also observed within the pearlite colonies at pearlitic cementite/ferrite interfaces. They also noted the different morphologies of the ferrite/austenite front and the preferential growth of austenite towards one specific neighboring pearlite colony. Li et al. [16] presented a crystallographic study indicating that austenite preferentially nucleates at the high angle boundaries of pearlitic ferrite and it preferentially grows into the adjacent pearlitic ferrite.

On the other hand, advances in computer simulations of phase transformations enable the understanding of the effect of different

* Corresponding author.
E-mail address: v.mattosferreira@tudelft.nl (V. Mattos Ferreira).

https://doi.org/10.1016/j.commatsci.2023.112368
Received 11 April 2023; Received in revised form 3 July 2023; Accepted 4 July 2023
Available online 14 July 2023

Table 1
Chemical composition of R260Mn steel.

Element	C	Mn	Si	Cr	P	S	V
wt.%	0.64	1.40	0.29	0.03	0.01	0.01	0.001

conditions on the phase transformation kinetics and morphology. Several studies have analyzed the austenite formation from a pearlitic microstructure using different modeling approaches [14,17–19].

Phase field modeling (PFM) has the advantage of enabling the simulation of complex growth morphologies [20]. However, not many studies have reported the use of PFM for simulating austenite formation from an initial pearlitic structure. Savran [21] and Thiessen et al. [22] simulated austenite formation from a ferrite-pearlite microstructure but considered pearlite as supersaturated ferrite with eutectoid carbon content. On the other hand, Rudnizki et al. [23] used the same approach while considering pearlite as a phase with mixed properties of ferrite and cementite. Other studies [21,24,25] considered the resolution of the cementite lamellae in the pearlite but in a very small domain only containing two to a maximum of five lamellae in the initial microstructure. Finally, Militzer et al. [26] simulated austenite formation from a 2D and 3D pearlitic structure taking into account the resolution of the cementite lamellae. However, no presence of pro-eutectoid ferrite was considered, and to avoid more complexity, the nucleation behavior as well as its influence was not analyzed in their work.

The focus of the present work is on the microstructural development during the wheel and rail contact due to thermo-induced phase transformation without incorporating the effect of plastic deformation. In order to do so, the austenitization of an initial pearlitic microstructure is simulated using the phase field model for two different heating rates: 10 and 200 °C s^{-1}. The initial domain consists of a pro-eutectoid ferrite grain which is surrounded by three pearlite colonies with approximately twenty cementite lamellae each. The domain size is chosen to resolve the features of cementite lamellae within a pearlite colony within reasonable limits for the computational time. The austenite growth kinetics and morphology obtained via simulation are compared with dilatometry and microscopic observations. Moreover, the influence of γ/θ and γ/α mobilities on the morphology is studied.

2. Material and experimental procedure

In this study, experiments were performed on R260Mn pearlitic railway steel which is commonly used in the Dutch railway network. This steel grade has a close-to-eutectoid chemical composition as exposed in Table 1 with the main alloying elements being C, Mn, and Si. XRD analysis shows the presence of 89% BCC phase (ferrite) and 11% cementite. Fig. 1 shows the Fe-C phase diagram for the constant values of Mn and Si concentrations, calculated using Thermo-Calc version 2021b with TCFE11 database [27]. The dashed vertical line represents the carbon concentration of R260Mn steel (0.64 wt%) and provides an estimation for the A_1^- and A_3 temperatures for equilibrium conditions, respectively equal to 705 °C and 730 °C, as indicated by the arrows.

Scanning Electron Microscopy (SEM) shows the presence of pearlite colonies as well as a small fraction of pro-eutectoid ferrite decorating the prior-austenite grain boundaries (Fig. 2), which results from a slight deviation from the eutectoid composition as shown in Fig. 1. From the SEM analysis in Fig. 2b, an estimation for the interlamellar spacing and cementite lamella thickness of approximately 150 and 20 nm is obtained, respectively.

The values of the equilibrium transition temperatures, A_1^- and A_3, served as guidelines for the design of dilatometry experiments with low and high heating rates. In order to investigate the kinetics of pearlite transformation during fast heating, dilatometric tests were performed in a Bähr 805 A dilatometer. This instrument uses an induction coil to heat the sample and detects the length change of the sample with a linear variable displacement transducer. The power supply is adjusted

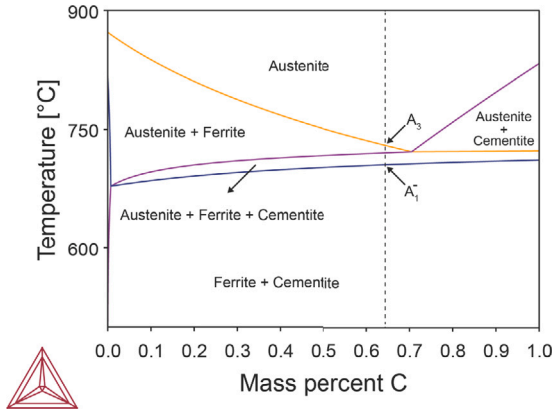

Fig. 1. Fe-C phase diagram for R260Mn steel obtained using Thermo-Calc software. The dashed line at 0.64 wt% C represents the carbon concentration in the studied alloy. Black arrows indicate the estimation for A_1^- and A_3 temperatures under equilibrium conditions.

to maintain the desired heating rate. Flat specimens with 1.5 mm thickness, 4 mm width, and 10 mm length were machined from the rail piece with the length coinciding with the running direction of the rail. Two thermocouples were spot welded at the center (TC1) and edge (TC2) of the specimen length, to investigate the temperature homogeneity in the sample during the test. The temperature control is based on TC1.

A first heat treatment (H_T) was carried out by heating the specimen with a high heating rate (200 °C s^{-1}) up to 900 °C (170 °C above the equilibrium A_3 temperature) followed by quenching. This heat treatment was performed to determine A_{c1} and A_{c3}, and therefore the overheating required for the pearlite transformation with respect to the equilibrium transition temperatures due to fast heating. As will be explained in section 3, the kinetics of the pearlite to austenite transformation at high heating rates cannot be extracted from the dilatometer curve of the specimen subjected to rapid heating. In order to overcome this, an additional heat treatment (L_T) with a lower heating rate (10 °C s^{-1}) up to 900 °C was performed, aiming at deriving the transformation kinetics to fit the simulation results.

Interrupted heating was performed to examine the microstructural features of austenite during the early stages of transformation. For this reason, two additional heat treatments with high and low heating rates were performed with the heating stage interrupted at the onset of the pearlite to austenite transformation, slightly above the A_{c1} temperature, followed by quenching. The goal of this set of experiments is to obtain small fractions of martensite (austenite at high temperatures), which are important for understanding austenite morphology in the early stages of phase transformation and will serve as guidelines for validating the simulation results. It also makes it possible to compare the austenite formed at high and low heating rates. The microstructural features were observed using a JEOL JSM-6500F scanning electron microscope after standard metallography sample preparation followed by chemical etching with Nital 2%. The microstructural analyses were done in the vicinity of TC1 where the maximum temperature prior to quenching is measured. Throughout the paper the specimen identification has been done in the following manner: A_z with A being the type of heating rate (H or L) and z the peak temperature (in °C) reached prior to quenching.

3. Experimental results

Fig. 3a shows the dilatation and austenite fraction as a function of temperature for sample H_{900} where a sharp increase of the dilatation signal is observed at 773 °C. A detailed explanation of the possible cause of this peak can be found in [28]. In summary, there is a

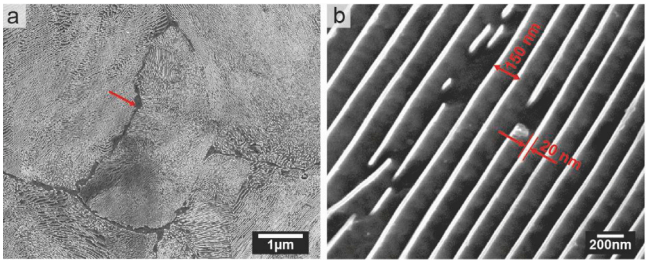

Fig. 2. SEM micrographs of the as-received R260Mn railway steel (a) evidencing the pearlitic microstructure with the red arrow indicating pro-eutectoid ferrite at the grain boundaries and (b) higher magnification micrograph showing the interlamellar spacing and lamella thickness.

temperature difference of approximately 60 °C between the middle (TC1) and the edge (TC2) of the dilatometry sample. Besides, the Curie temperature of this steel (757 °C) coincides with the onset of austenite formation at high heating rates. When the center of the specimen reaches the Curie temperature (757 °C), the edge of the sample is still 60 °C below this temperature. Therefore, when the controlling thermocouple located in the center of the sample crosses this temperature, the equipment increases the power input to maintain the high heating rate. This causes a sharp increase in the heating rate at the edge of the sample where the material is still ferromagnetic and consequently the anomalous peak, due to thermal expansion, in the dilatation curve. Unfortunately, this sharp increase of the dilatation coincides with the start of austenite formation, and that makes it impossible to precisely derive the value of A_{c1}, as is usually done from the deviation of the linearity of the dilatation curve. This peak also interferes with the calculation of the phase fraction formed, especially at the temperature range highlighted with a light gray rectangle in Fig. 3a, where the temperature gradient and heating rates are substantially different between the central and edge regions. However, the later stage of phase transformation kinetics (after 50% of austenite is formed) will still be considered as a reference for the simulations. In this case, we assume that a delay takes place due to thermal gradients which can be estimated by the temperature difference between TC1 and TC2 at approximately 11 °C after the pearlite is fully transformed to austenite. At temperatures above the peak, the decrease in the dilatation signal reflects the ongoing pearlite-to-austenite transformation. The transformation is complete at approximately 805 °C, the value assigned to A_{c3} for a heating rate of 200 °C s^{-1}. Fig. 3b presents the dilatation signal and phase fraction of austenite formed for sample L_{900}, subjected to the lower heating rate of 10 °C s^{-1}. As can be seen, both A_{c1} and A_{c3} are lower than for sample H_{900}. This means that a higher overheating is necessary for austenite to form at 200 °C s^{-1} than at 10 °C s^{-1}. The influence of the heating rate and the intercritical temperature shift has been previously reported in the literature [29].

Fig. 3c shows the temperature profiles recorded from the two thermocouples welded to the samples subjected to intercritical heating with different heating rates (H_{751} and L_{745}) followed by quenching. The peak temperatures measured at the location of TC1 were 751 °C and 745 °C. As these samples were subjected to heating up to the early stage of austenite formation, there is no discernible divergence from linearity in the dilatation curves. This is due to the limitation of the equipment to detect such a small fraction of phase transformation in both heating and cooling curves.

The microstructures of samples H_{751} and L_{745} were examined using SEM to determine the presence of small martensitic patches (austenite at high temperatures). These patches provide knowledge on the nuclei sites and early growth behavior of austenite, which is necessary to further investigate the microstructural aspects of austenite formation using phase field simulations. Fig. 4 shows a series of micrographs of regions containing transformed patches of martensite in H_{751} (a-f) and L_{745} (g-i). Overall, the growth morphology of austenite is quite similar for both samples. The martensite patches observed are not homogeneously distributed in the microstructure but rather situated in preferential locations, such as at pro-eutectoid ferrite boundaries (Fig. 4a,b), inside pearlite colonies (Fig. 4d,e,g,h) and at the pearlite colonies' boundaries (Fig. 4c,f,i). These preferential sites for austenite nucleation and growth in pearlitic microstructures have been previously reported in the literature for different heating rates [16,30].

An additional aspect that can be extracted from these micrographs is the growth morphology of austenite at the onset of the pearlite to austenite transformation. The martensite patches that nucleated at the boundaries show a similar pattern of growing towards the bulk of a preferential pearlite colony. This trend is observed in Fig. 4c where the austenite grows mainly towards one specific colony of pearlite. Fig. 4b shows an enlarged portion containing a martensite patch. The martensite front (austenite at high temperature) presents a sharp shape, growing preferentially along the cementite lamellae (white arrow). That is reasonable as cementite is richer in carbon than ferrite and thus plays an essential role during austenite growth at high temperatures. On the other hand, the enlarged region in Fig. 4e accounts for another growth mechanism highlighted by a white arrow. In this case, the austenite front is much flatter between the two cementite lamellae. Moreover, in this case, regions with thinner cementite lamellae can be observed (black arrow) which are due to partial transformation of cementite during the austenitization process. These findings have been previously reported in the literature by Shtansky et al. [15].

In summary, the main microstructural features of austenite growth in pearlite are:

- Growth along cementite lamellae (sharp front);
- Growth along ferrite (flat front);
- Preferential growth towards a pearlite colony;
- Undissolved cementite inside austenite.

4. Phase-field modeling

4.1. Phase-field theory

The multi-phase field model proposed by Steinbach et al. [31] and extended to multicomponent alloys by Eiken et al. [32] is used to simulate the growth of austenite from an initial pearlitic microstructure. In this approach, each grain (i) is described by the so-called phase-field parameter, $\phi_i(\vec{x},t)$, which can assume the value of 1 if the grain i is present at a location $\vec{x}$ and time t or the value of 0 if the grain i is not present. The field parameter varies smoothly at the grain boundaries from 0 to 1 over a diffuse transition region of width η. In addition, each grain has a set of attributes that are relevant for describing the transformation of interest such as the lattice structure (phase) and the crystallographic orientation. In the case of a multi-component alloy, a concentration vector $\mathbf{c}(\vec{x},t)$ is defined to describe the local composition of alloying elements:

$$c^k(\vec{x},t) = \sum_{i=1}^{v} \phi_i c_i^k(\vec{x},t) \tag{1}$$

with v being the number of coexisting grains at location $\vec{x}$ and c_i^k the concentration of solute k in the individual grain i. The time evolution of v phase-field parameters describes the kinetics of the phase transformation and it is obtained by solving the following phase-field equations:

$$\dot{\phi}_i = \sum_{j\neq i}^{v} M_{ij}^{\phi}\left[b\Delta G_{ij} - \sigma_{ij}K_{ij} + \sum_{\substack{j\neq i \\ j\neq k}}^{v} J_{ijk}\right] \tag{2}$$

where M_{ij}^{ϕ} is the phase-field mobility of the interface between grains i and j, b a numerical weight constant, ΔG_{ij} the thermodynamic driving force, σ_{ij} the interfacial energy between grains i and j, K_{ij} the pairwise

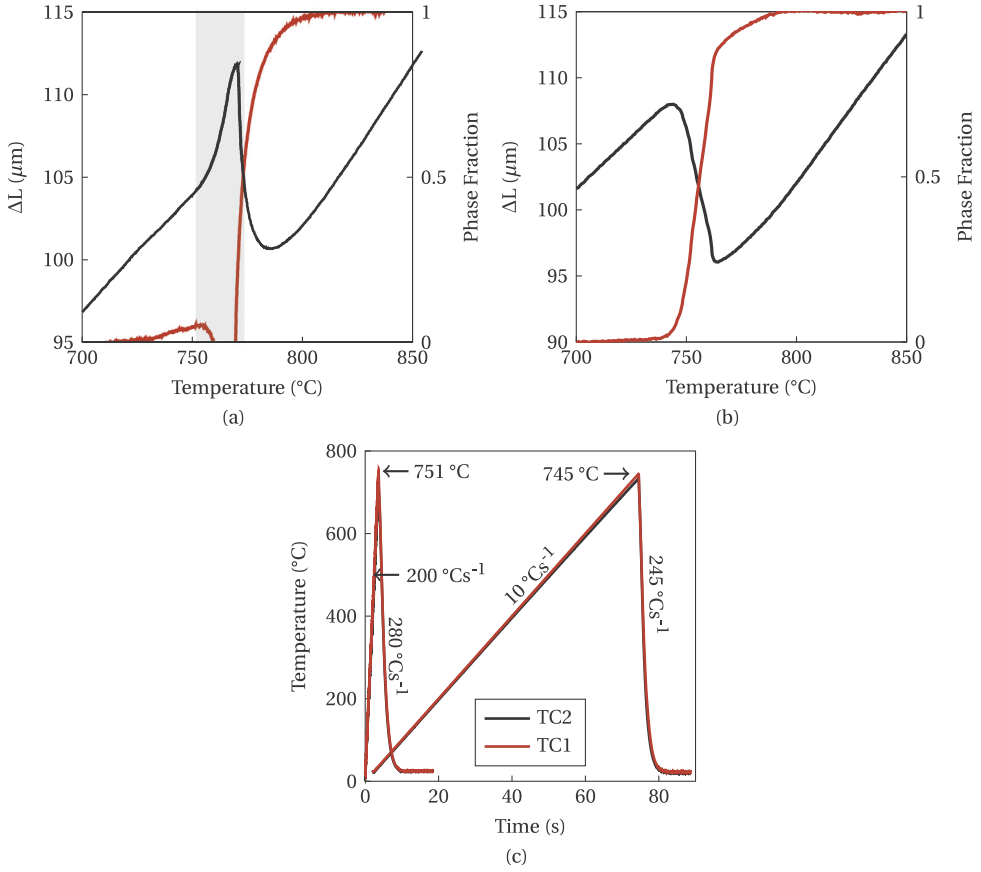

Fig. 3. Dilatation and austenite phase fraction as a function of temperature for samples (a) H_{900} and (b) L_{900}; (c) Time–temperature graph of L_{745} and H_{751} subjected to intercritical austenitization followed by quenching.

curvature contribution and J_{ijk} the triple junction term, which is zero for $\upsilon = 2$. The driving force in Eq. (2) depends on the local composition $\mathbf{c}(\vec{x}, t)$. Therefore, Eq. (2) is solved coupled with a set of diffusion equations, given by

$$\frac{\partial c^k}{\partial t} = \nabla \sum_{i=1}^{\upsilon} \sum_{l=1}^{\xi} \phi_i D_i^{kl} \nabla c_i^l \tag{3}$$

$$D_i^{kl} = \sum_{m=1}^{\xi} M_i^{ch,km} \Phi_i^{ml} \tag{4}$$

in which ξ is the number of alloying elements and Φ_i^{ml} denotes thermodynamic factors used to convert the chemical atomic mobilities $M_i^{ch,km}$ into diffusivity D_i^{kl} [32].

The phase-field model is derived as a growth model, in which the nucleation behavior is considered depending on the input density, distribution, and growth rate of the nuclei [33]. In commercial software such as MICRESS®, the nuclei density is controlled by two main parameters: shield distance and shield time. The shield distance defines the minimum distance between nuclei formed within the shield-time interval. The shield time controls the formation of new nuclei, which is only allowed at the onset of a shield-time interval. For example, if a shield time t is and shield distance d are considered, simultaneous nucleation will only occur at every time interval t with a minimum distance of d between the nuclei. The nucleation occurs when the local overheating (calculated by Thermo-Calc based on the local composition) is higher than the overheating required for nucleation, which is one of the input parameters.

4.2. Simulation conditions

2D phase-field simulations were performed to study the pearlite to austenite transformation in an Fe - 0.64 wt% C - 1.4 wt% Mn ternary alloy during heating at 10 and 200 °C s^{-1}. The MICRESS® (version 7.123, Access e.V., Aachen, Germany) software [34] was used to solve the phase-field equations (Eq. (2) coupled with Eq. (3)) and enable the simulation of microstructure morphology and alloy element distribution in time and space.

The construction of the simulated initial microstructure is done by taking the 2D SEM micrograph (Fig. 2a) as a reference, see Fig. 5. However, the large domain from the SEM micrograph would impose a challenge in resolving the cementite lamellae because of the extensive simulation time. Due to this limitation, a smaller domain of approximately 6x × 6 μm^2 is considered as the initial microstructure. As can be seen from Fig. 5, the domain contains the boundary region of three pearlite colonies with the resolved cementite lamellae parallel to each other within each colony. In one portion of the colonies, some gaps were placed between cementite segments, one of which is highlighted with a black arrow. This feature is incorporated to take into account the discontinuities observed in the pearlite as it is not a perfectly continuous structure. The interlamellar spacing corresponds to the one measured in the as-received material (150 nm). Moreover, the presence of pro-eutectoid ferrite in the boundary region observed in the SEM micrograph (Fig. 2) is also taken into account.

The grid size was set to 0.01 μm with the interface thickness (η) corresponding to three grid cells. Isolated boundary conditions were assumed in all simulations. The composition of ferrite and the cementite lamellae was set equal to the equilibrium conditions at 700 °C. The temperature profile applied for dilatometry experiments was employed. The only modification is that the beginning temperature for the simulation is set to 735 °C and 719 °C for 10 °C s^{-1} and 200 °C s^{-1}, respectively, in order to shorten simulation time as no phase transformation occurs below these temperatures.

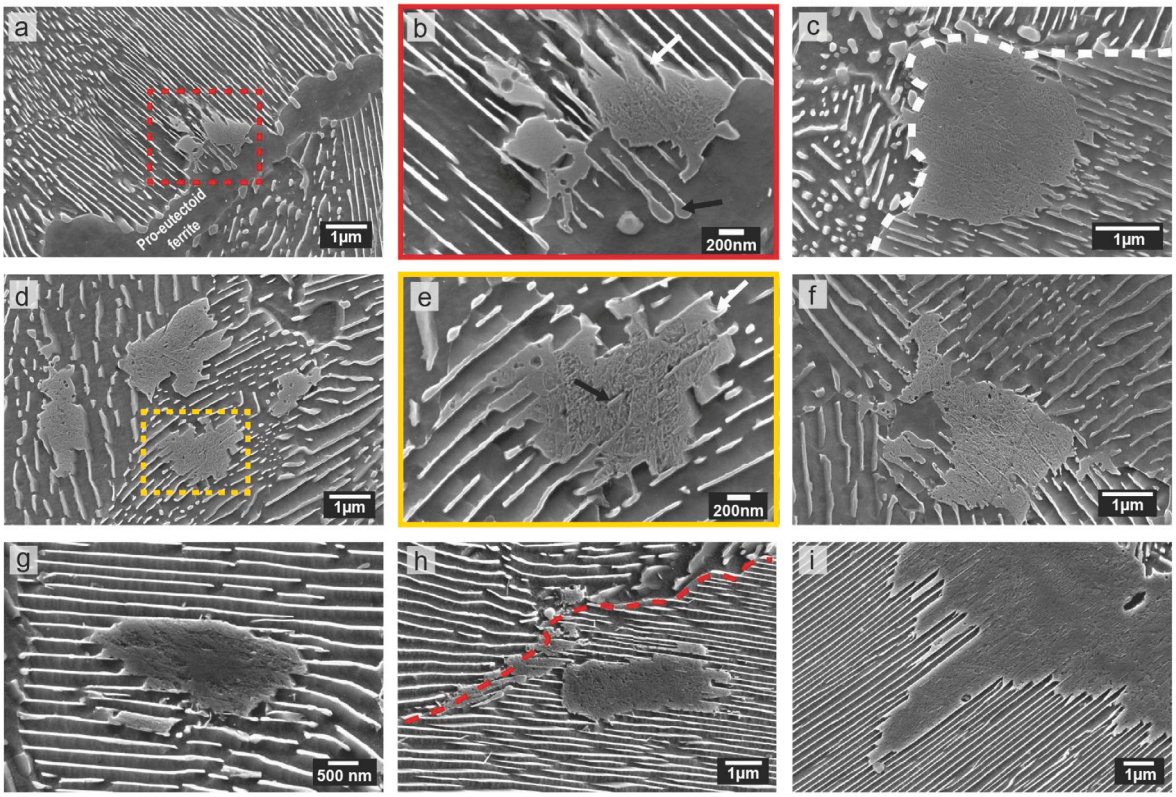

Fig. 4. Scanning electron microscopy image of martensitic patches found in samples H_{751} (a-f) and L_{745} (g-i). White arrows in (b) and (e) indicate sharp- and flat-front growth of austenite, respectively. Black arrows in (b) and (e) show the nuclei of austenite and the undissolved cementite, respectively. Dashed lines in (c) and (h) highlight the pearlite boundary.

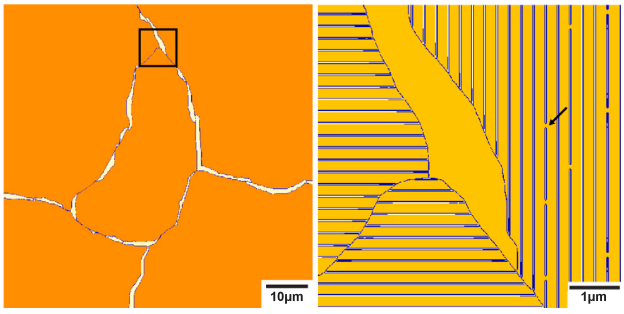

Fig. 5. Initial microstructure with the resolved cementite lamellae in the pearlitic microstructure used in the phase field simulations.

Table 2 presents the kinetics parameters assumed in the simulations. The α/α, α/θ, and γ/γ interface mobilities are considered to be very low in order to limit the study to the analysis of γ/α and γ/θ interfaces. For γ/α and γ/θ interfaces, the mobility is considered to be temperature dependent according to the Arrhenius relation:

$$M = M_0 \exp\left(-\frac{Q}{RT}\right) \tag{5}$$

where Q is the activation energy for interface motion (140 kJmol^{-1} [35]), R the gas constant (8.31 JK^{-1}mol^{-1}) and M_0 the pre-exponential factor. The pre-exponential factor and, consequently, the mobilities of the γ/θ and γ/α interfaces play an important role in the final morphology of the austenite front. The same counts for the interface energies. However, accurate values of mobility and interfacial energy are still missing. For this reason, values in the same order of magnitude as reported in the literature [36,37] were chosen, considering that the microstructural evolution is in agreement with the experimental observations. The interfacial energies and the pre-exponential factor values of the mobilities of the different grain boundaries and interfaces are reported in Table 2.

MICRESS® also requires input parameters for the nucleation of austenite nuclei such as the maximum number of nuclei, shield time, and shield distance. The combination of these parameters defines the nuclei density, which can strongly affect the final result, especially for simulations with small domains. In the current study, all simulations considered two possible nucleation sites for austenite:

- at α/α grain boundaries (pro-eutectoid ferrite/pearlitic ferrite or pearlitic ferrite/pearlitic ferrite);
- at α/θ interfaces (pro-eutectoid ferrite/cementite or pearlitic ferrite/cementite).

The simulations consider a very small pearlitic domain which makes it impossible to obtain a good estimation for the austenite grain sizes and relate these to the experimental values. As a result, no correlation can be made between the experimental grain sizes and the nucleation rate [38]. Consequently, the nucleus density together with interface mobility was set in order to fit the phase fraction curve for each simulation.

MICRESS allows the attribution of a parameter θ for each grain in 2D simulations. This parameter can be used to control the anisotropy of the mobility in order to accomplish non-isotropic growth of grains. In this paper, when a new austenite nucleus is set at the boundary of two colonies, a θ value is assigned to it. MICRESS code allows assigning to a new grain a θ value which is related to θ of one of the two neighboring parent ferrite grains, randomly selected. As a result of the assumed anisotropy, the nuclei exhibit a distinctive growth pattern, predominantly growing towards a specific pearlite colony rather than displaying isotropic growth.

Thermodynamic data are required to evaluate from the local concentration the overheating to set the nuclei of the austenite phase (a

Table 2
Kinetic parameters used in the simulations with MICRESS®.

Interface	α/α	α/θ	γ/α	γ/θ	γ/γ
Interfacial energy (Jm^{-2})	0.70	0.50	0.60	0.40	0.70
Interface mobility ($m^4J^{-1}s^{-1}$)	5 x 10^{-16}	5 x 10^{-16}	$M(T)$	$M(T)$	5 x 10^{-16}

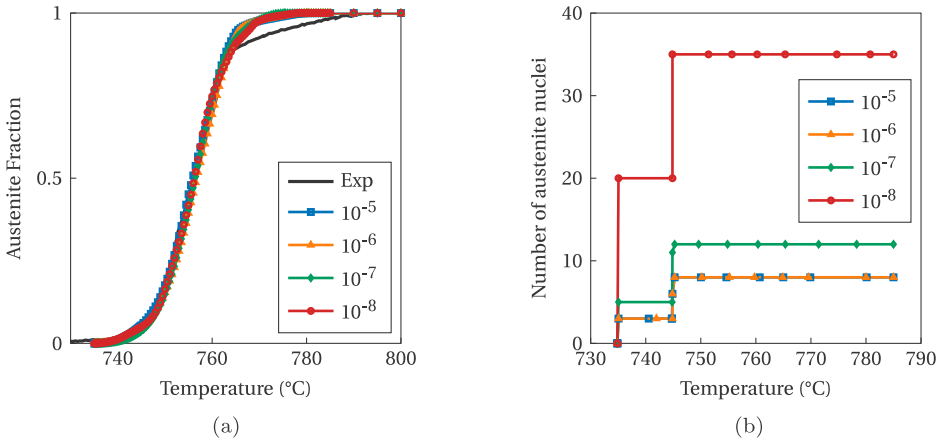

Fig. 6. (a) Austenite phase fraction as a function of temperature obtained experimentally (black solid curve) and via phase field simulation with different pre-exponential factors for γ/θ mobility (colored lines with symbols) and (b) Number of austenite nuclei as a function of temperature for each simulation with different pre-exponential factors of γ/θ mobility. The unit of the interface mobilities is $m^4J^{-1}s^{-1}$.

new nucleus is set when the critical nucleation overheating, assigned as an input parameter, is exceeded), the driving force for the austenite growth, and also the diffusivity and partitioning of the alloying elements into the coexisting phases in the diffuse interface under quasi-equilibrium constraint (equal chemical potential at the interface). The evaluation of this constraint is done by minimization of the multiphase Gibbs free energy, calculated from Calphad databases via the TQ-interface of the Thermo-Calc software.

4.3. Simulation results

4.3.1. Effect of γ/θ mobility

The two-dimensional (2D) phase-field simulations presented in this section aim at understanding the effect of the γ/θ mobility on the growth morphology of the austenite. To achieve this, the pre-exponential factor of the γ/α interface mobility ($M_0^{\gamma/\alpha}$) is set at a value equal to 10^{-6} $m^4J^{-1}s^{-1}$ while the pre-exponential factor of the γ/θ interface mobility ($M_0^{\gamma/\theta}$) varies for each simulation. Four values of $M_0^{\gamma/\theta}$ are considered, ranging from 10^{-8} to 10^{-5} $m^4J^{-1}s^{-1}$. It is important to note that the exact values of interface mobility and nucleation parameters are unknown. A strong correlation emerges when achieving agreement between experimental and simulated fraction curves.

The choice of parameters is based on fitting the austenite fraction of the simulations with different $M_0^{\gamma/\theta}$ conditions to the one obtained experimentally (Fig. 3b). A change in mobility leads to changes in the kinetics of the phase transformation. To overcome this, the nuclei density is adjusted for each simulation to obtain a good fit to the experimental results. As no experimental information regarding the nucleation rate is available, a shield time of 1.0 s is assumed as an input parameter for all simulations while the nuclei density is adjusted to obtain a proper kinetics representation. In addition, all simulations consider a heating rate of 10 °C s^{-1} in accordance with the experiment (Fig. 3b). This means that new nuclei are allowed to form at intervals equal to 1.0 s (10 °C intervals on the temperature scale).

Fig. 6a shows the austenite fraction as a function of temperature for the experimental and simulated conditions. As can be seen, the simulated curves accurately replicate the overall kinetics of the transformation observed experimentally. Fig. 6b presents the number of austenite nuclei as a function of temperature considered for each pre-exponential mobility factor. The nucleation occurs in two events for all simulations. The first happens at the onset of the simulation (735 °C) and is marked by a lower density of nuclei in order to achieve the slower kinetics observed at the beginning of the phase transformation, see Fig. 6a. The second nucleation event takes place at 745 °C which corresponds to the increase in the kinetics of austenite formation. The faster kinetics is due to an increase in austenite nuclei density and austenite/pearlite interface area. No further nucleation occurs until the end of the simulation and the kinetics is controlled only by the growth of the existing nuclei.

The analysis of the nuclei density in Fig. 6 shows that a further increase of the interface mobility above a threshold value does not require an adjustment of the nucleation setting to fit the kinetics, meaning that the austenite formation occurs under diffusion control. Diffusion during austenite formation will be discussed later, in Section 4.3.2. On the other hand, lower mobilities imply mixed-mode growth, so both interface mobility and diffusion play a significant role in the kinetics. For this, it is necessary to increase the nuclei density in order to compensate for the lower mobility such as observed for $M_0^{\gamma/\theta}$ equal to 10^{-7} and 10^{-8} $m^4J^{-1}s^{-1}$. In summary, austenite formation can be characterized as a mixed-mode transformation for lower mobilities ($M_0^{\gamma/\theta}$ equal to 10^{-7} and 10^{-8} $m^4J^{-1}s^{-1}$) but shifts towards diffusion controlled for higher mobilities ($M_0^{\gamma/\theta}$ equal to 10^{-6} and 10^{5} $m^4J^{-1}s^{-1}$).

The dilatometry results highlight a decrease in the kinetics of austenite formation at the final stages of the austenite formation, see Fig. 6a. This behavior is attributed to the growth of austenite into the pro-eutectoid ferrite which occurs at a much lower rate than into pearlite due to long-range carbon diffusion [39]. For this reason, the pro-eutectoid ferrite regions are expected to transform to austenite at a later stage and at a lower rate than the pearlite. However, it is not possible to fully control the nuclei positions in the simulation nor differentiate between austenite/pro-eutectoid ferrite and austenite/pearlitic ferrite interfaces. This leads to nucleation and growth occurring in the pro-eutectoid ferrite at 745 °C, reducing its effect by the end of the simulation. Although it was not possible to fit the simulation curves properly in this portion of the experimental curve, a reduction of the kinetics was still achieved, providing a good representation of the change in kinetics.

In Fig. 7, the simulated microstructure evolution at 750 °C (a) and 760 °C (b) for different $M_0^{\gamma/\theta}$ are depicted. These stages are representative of the early and intermediate stages of austenite formation.

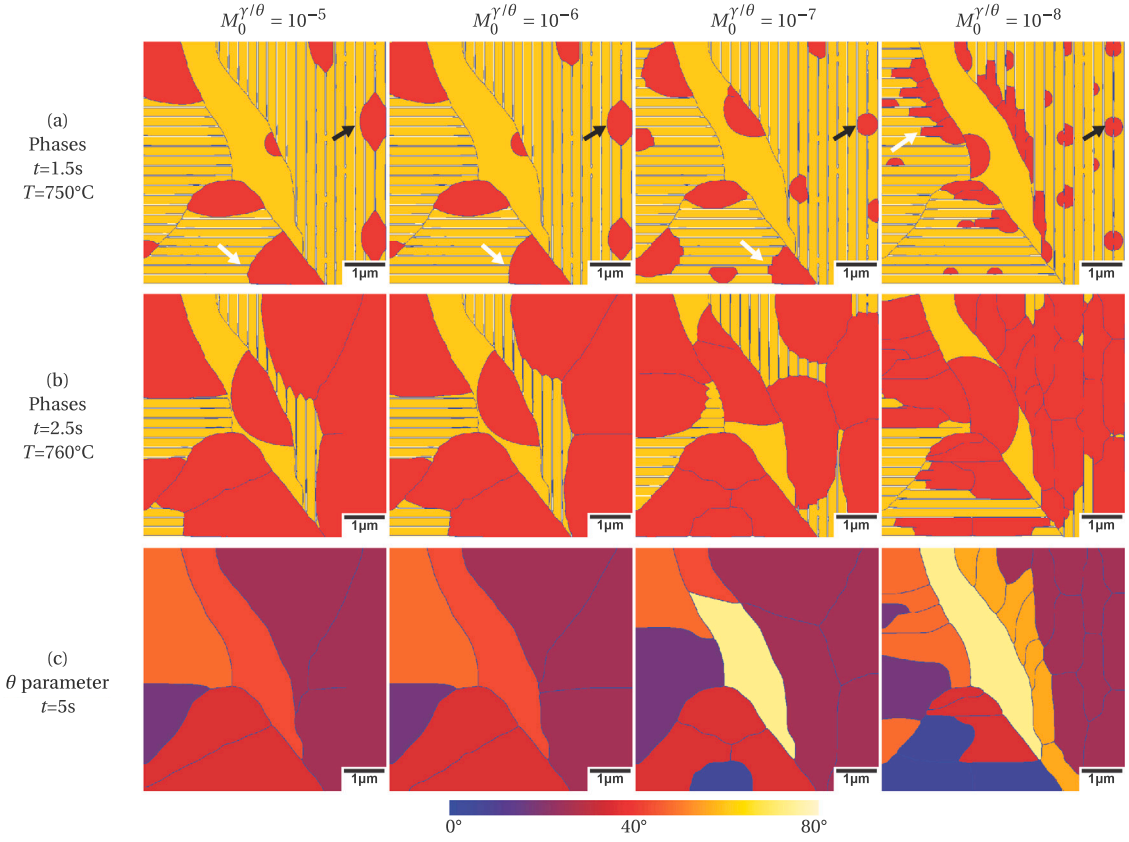

Fig. 7. (a,b) Simulated microstructural evolution at t = 1.5 s and 2.5 s for different γ/θ pre-exponential factors ($M_0^{\gamma/\theta}$) with red grains representing the austenite phase. (c) θ parameter for t = 5 s (fully transformed microstructure) for different $M_0^{\gamma/\theta}$ ($m^4J^{-1}s^{-1}$), with colors indicating the θ parameter (see Section 4.2).

At 750 °C differences are seen in the growth morphology of austenite (red grains) due to differences in mobility. For higher values of $M_0^{\gamma/\theta}$, the grains nucleated within the pearlite (black arrows) show a sharp front that has also been observed experimentally, see Fig. 4b. This morphology changes to a more equiaxial round shape by decreasing $M_0^{\gamma/\theta}$. For $M_0^{\gamma/\theta}$ equal to 10^{-8} $m^4J^{-1}s^{-1}$, the cementite is encapsulated by the surrounding austenite (see black arrow in Fig. 7a) instead of being completely transformed, such as observed for the other cases.

The nuclei located at the colony boundaries (white arrows) not only grow towards the bulk of the pearlite colony but also along the colony boundaries. The preferential growth towards one specific pearlite colony is due to the mobility anisotropy considered in this study and is in accordance with experimental observations. The growth front of these nuclei has a more continuous appearance for higher mobilities, suggesting that the austenite front moves at approximately the same rate as the cementite dissolution. On the other hand, lower γ/θ interface mobilities lead to a flat austenite growth front. In this case, the austenite grows preferentially into the ferrite within two adjacent cementite lamella due to the higher mobility of the γ/α interface. In this case, the velocity of the γ/θ interface is reduced, leading to a delay of the cementite dissolution with the growth of austenite. This flat growth is also experimentally evidenced in partially transformed pearlite microstructures, see Fig. 4e.

At the end of the simulation, both pearlite and pro-eutectoid ferrite are transformed into austenite. The θ parameter of the final grains is depicted in Fig. 7c. Adjacent austenite grains with the same θ parameter can appear in micrographs as a single austenite grain which was transformed into martensite during quenching. As expected, the nuclei density has a clear effect on the final austenite grain size. As previously mentioned, lower mobility requires a higher nuclei density in order to achieve the same kinetics. Consequently, the austenite grain size decreases with decreasing mobility. The morphology of the grains is also influenced in this case, changing from a more polygonal to an elongated shape during the phase transformation.

4.3.2. Diffusion processes

Fig. 8 shows the carbon profile in γ and α of a small portion of the simulated microstructure for the highest and lowest $M_0^{\gamma/\theta}$ mobilities at 743 and 751 °C, respectively. As can be seen, carbon concentration gradients in γ and α are present regardless of the interface mobility. For high mobilities, a sharp austenite front is observed with higher carbon contents at the γ/θ interface region while lower carbon contents are present at the γ/α interface. At this condition, carbon does not have enough time to homogenize in the fast-growing austenite, which leads to carbon concentration gradients within the austenite grain. As cementite is the main carbon source for austenite growth, the locations near cementite are enriched in carbon.

On the other hand, if the lowest $M_0^{\gamma/\theta}$ is considered, the austenite front has a flat shape. In this case, the front growth is compromised as the rate of cementite dissolution is lower than the formation rate of austenite from ferrite, leading to the carbon source (cementite) being located behind the austenite growth front. Also in Fig. 8, the carbon content in α is depicted. While a slight enrichment of α is seen for both mobilities, a bigger variation is seen for the higher mobility.

To have a better insight into the carbon distribution behavior in austenite during growth, the carbon concentrations at γ/α and γ/θ interfaces were analyzed for the simulation with high γ/θ mobility ($M_0^{\gamma/\theta} = 10^{-5}$ $m^4J^{-1}s^{-1}$). Fig. 8b displays the carbon content in γ at T = 739.65 °C. As can be seen, the austenite nucleus has mainly grown along the cementite lamella at which it nucleated and laterally towards the neighboring pearlitic ferrite. Above this temperature, the growing austenite encounters an additional carbon source in the adjacent cementite lamella at the top right-hand corner of Fig. 8b, highlighted with a white arrow. This leads to γ being saturated in carbon at this location

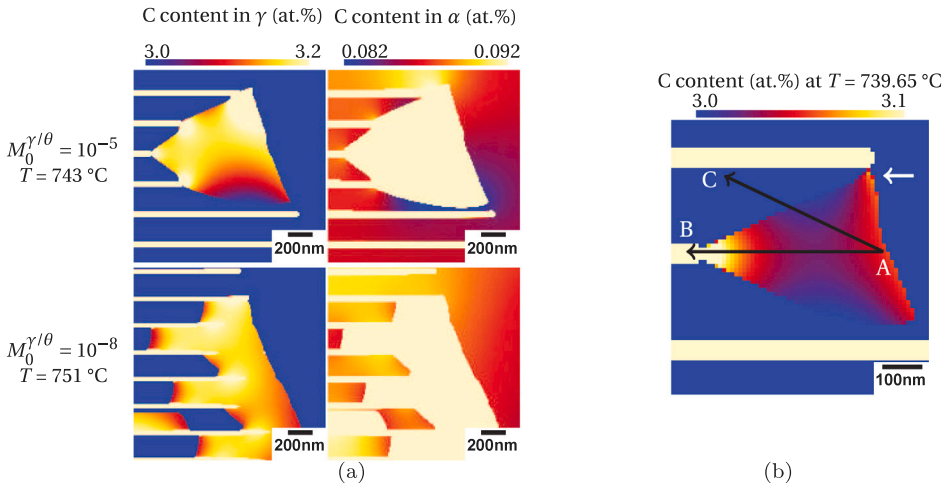

Fig. 8. (a) Carbon content in austenite (γ) and ferrite (α) for highest and lowest $M_0^{\gamma/\theta}$ ($m^4J^{-1}s^{-1}$); (b) Carbon content in γ at T = 739.65 °C for simulation with $M_0^{\gamma/\theta} = 10^{-5}$ $m^4J^{-1}s^{-1}$.

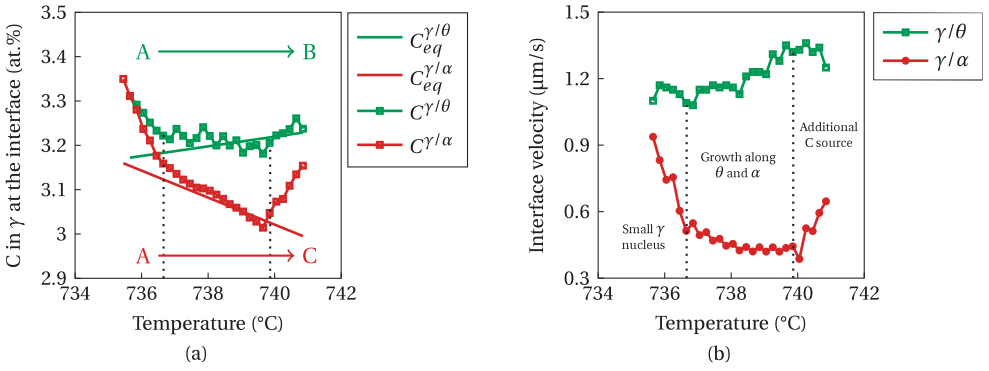

Fig. 9. (a) Carbon concentration in γ at the γ/θ interface along A-B line (see Fig. 8b) and γ/α interface along A-C line (see Fig. 8b) and the respective equilibrium values as a function of temperature; (b) Velocity of γ/θ (along A-B line) and γ/α (along A-C line) interfaces as a function of temperature.

and consequently changes the carbon concentration gradients within γ. Due to the complex topology of the pearlitic structure with additional carbon sources playing a role in the austenite growth at different time steps, a representation of the overall growth of γ is impossible. For this reason, two line profiles are chosen to represent the local behavior of γ/θ (A-B line) and γ/α (A-C line) interfaces, represented by black arrows in Fig. 8b. Fig. 9a presents a comparison between the carbon content in equilibrium and the carbon content obtained via simulation at the γ/θ and γ/α interfaces. The equilibrium carbon contents ($C_{eq}^{\gamma/\theta}$ and $C_{eq}^{\gamma/\alpha}$) are calculated based on the linearization data of the Fe-C-Mn phase diagram provided at the onset of the MICRESS simulation. The plotted interface values consider the carbon content of the last austenite point prior to the diffuse interface region along both A-B ($C^{\gamma/\theta}$) and A-C ($C^{\gamma/\alpha}$) lines for different temperatures. Fig. 9b shows the interface velocity of both γ/θ (A-B) and γ/α (A-C) interfaces as a function of temperature. The overall velocity of the γ/θ interface is much higher than the one observed in the case of γ/α due to its proximity to the carbon source.

As can be seen from Fig. 9a, the austenite is supersaturated in carbon at both γ/θ and γ/α interfaces up to approximately 737 °C. This is due to the small size of the γ nucleus in the vicinity of θ (carbon source) leading to local enrichment of γ and additional driving force for the interface movement of austenite into the low-carbon ferrite. For this reason, a higher interface velocity is observed for the γ/α interface at this temperature range and it decreases with the growth of the austenite nucleus and the consequent decrease of carbon content towards equilibrium.

From 737 °C to approximately 739 °C, the carbon content at both interfaces stabilizes around the equilibrium value as the austenite grows both along the cementite (carbon source) and ferrite (low in carbon). In this region, the interface is expected to move at a rate controlled by carbon diffusion within the austenite and the velocity stabilizes. However, this behavior changes for temperatures above 739 °C where an increase of the carbon content and the velocity of the γ/α interface are observed. Fig. 10a shows the carbon content in austenite at 739.45 and 739.85 °C with D-E and D'-E' lines located parallel to the moving γ/α interface between two cementite lamellae. The carbon profiles along these two lines are plotted in Fig. 10b. At 739.45 °C, γ is enriched in carbon at the vicinity of point D (carbon source) and a gradual decrease of carbon is seen towards point E due to lack of time for the carbon to homogenize in γ. However, at 739.85 °C, both D' and E' regions are enriched in carbon. At this point, the austenite reaches an additional carbon source at the neighboring cementite lamella. This carbon diffuses towards the low-carbon austenite near the γ/α interface, causing an increase of the carbon content at the γ/α interface, see Fig. 9a. As a result, an increase in the velocity of the γ/α interface is observed, as shown in Fig. 9b.

4.3.3. Effect of γ/α mobility

In this section, the effect of γ/α mobility on the transformation kinetics is presented. To so do, the γ/θ mobility was considered equal to 10^{-6} $m^4J^{-1}s^{-1}$ while variations of γ/α interface mobility were implemented. It was noted that one order of magnitude changes in γ/α mobility lead to a substantial increase in the kinetics of phase transformation and consequently impossibility to fit the experimental

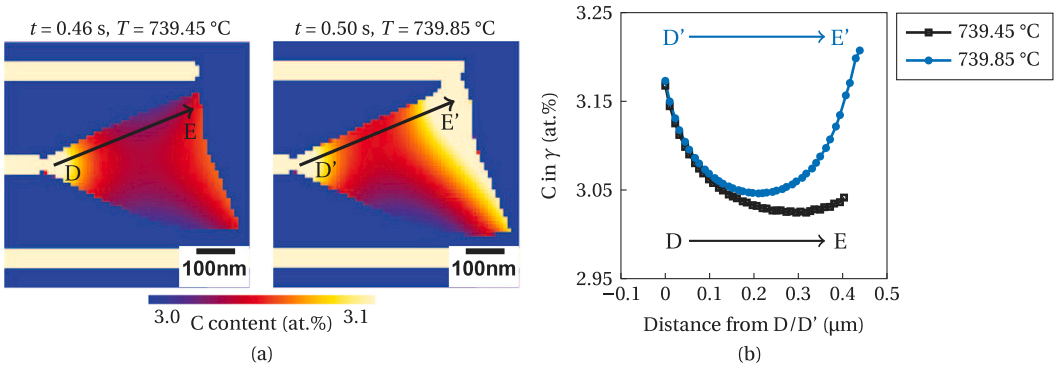

Fig. 10. (a) Carbon content in γ at 739.45 °C and 739.85 °C for simulation with $M_0^{\gamma/\theta} = 10^{-5}$ m^{4}J^{-1}s^{-1}. (b) Carbon profile in γ across D-E line (T = 739.45 °C) and D'-E' line (T = 739.85 °C).

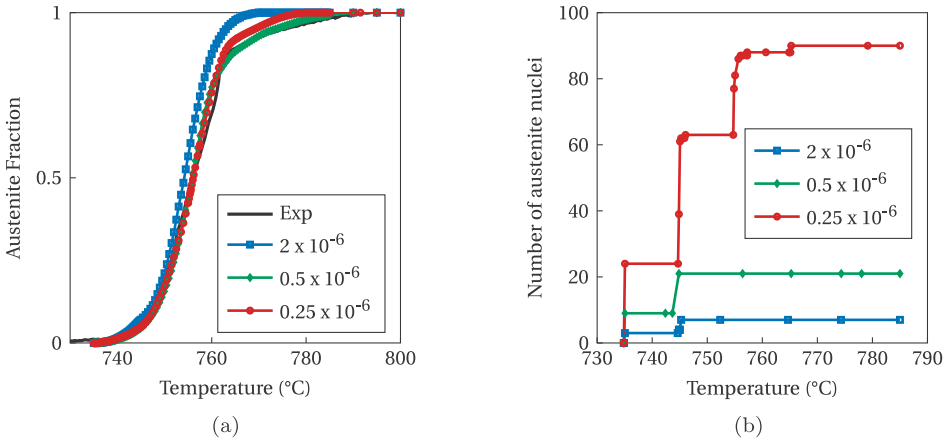

Fig. 11. (a) Austenite phase fraction as a function of temperature obtained experimentally (black solid curve) and via phase field simulation with different pre-exponential factors for γ/α mobility (colored lines with symbols) and (b) Number of austenite nuclei as a function of time for each simulation with different pre-exponential factors of γ/α mobility (m^{4}J^{-1}s^{-1}).

curves. For this reason, lower variations of this interface mobility are assumed for this study.

In Fig. 11a the simulated and experimental austenite fraction as a function of temperature is presented. With a low γ/α interface mobility it is possible to accurately fit the experimental curve, while high mobility imposes difficulties in fitting the curve, mainly at later stages of the phase transformation. Besides that, with a low mobility it is possible to properly capture the change in kinetics during pro-eutectoid ferrite transformation. In the pro-eutectoid ferrite region, only γ/α interfaces are present. By reducing the γ/α interface mobility, the movement of this interface is limited and will occur at a lower rate than γ/θ interface motion. Consequently, the growth rate into the pro-eutectoid ferrite will be lower than in the pearlite region where both interfaces are present, leading to a good correspondence with the experimental kinetics. The nuclei density corresponding to each condition is shown in Fig. 11b. A much higher nuclei density is needed if lower γ/α mobilities are considered. This reflects the effect of this mobility on the growth kinetics of austenite as the grains will grow at a lower rate and consequently new nuclei are allowed to form.

The changes in the microstructural features are seen in Fig. 12. In the case where the γ/α mobility is slightly higher than the γ/θ mobility, the flat growth front is observed. On the other hand, lower values of γ/α mobility relative to γ/θ mobility cause the sharp front growth morphology with the cementite being consumed at a considerably higher rate than the growth into the pearlitic ferrite. As the final austenite grains are related with the nuclei density, more polygonal shapes are seen for higher γ/α mobilities in which the nuclei density is low. In summary, the mobility of both γ/θ and γ/α interfaces influence the kinetics and morphology of austenite formation. In the real material, variations in mobility occur due to interface characteristics such as crystallographic orientation and local chemical composition. This is why different growth morphologies are seen in the real material (Fig. 4). The combination of these factors can lead to different microstructural features during austenite growth.

4.3.4. *Simulation with 200 ° Cs^{-1}*

This section presents the results obtained for a simulation with a heating rate of 200 °C s^{-1}. The simulation is set to start at 720 °C which is below the expected A_{c1} temperature. The mobility values of γ/α and γ/θ interfaces are 3.5 x 10^{-5} m^{4}J^{-1}s^{-1}. A higher mobility is needed in order to fit the experimental curve for higher cooling rates. This increase is required because MICRESS input mobility is not a representation of the intrinsic mobility of the interface but rather an effective parameter that incorporates the effects of various model simplifications [38]. This effective mobility can vary with the evolution of phases involved and various aspects have been reported to have an effect on the effective mobility in MICRESS, such as heating/cooling rates, grid size and space dimension of the simulations (2D or 3D) [38,40,41]. As the interface mobilities are assumed to be equal, the growth morphology shows a flat growth, see Fig. 13a.

In Fig. 13, the experimental and simulated phase fractions are compared. As explained in Section 3, the experimental phase fraction at high heating rates is affected by the thermal gradient of the dilatometry sample. However, it can still provide an estimation of the kinetics of the phase transformation at the later stages of transformation as depicted in Fig. 13c. At first glance, it appears that the simulation occurs with higher kinetics than the experiments. As indicated in Section 3, a temperature lag of 11 °C is estimated for experiments with 200

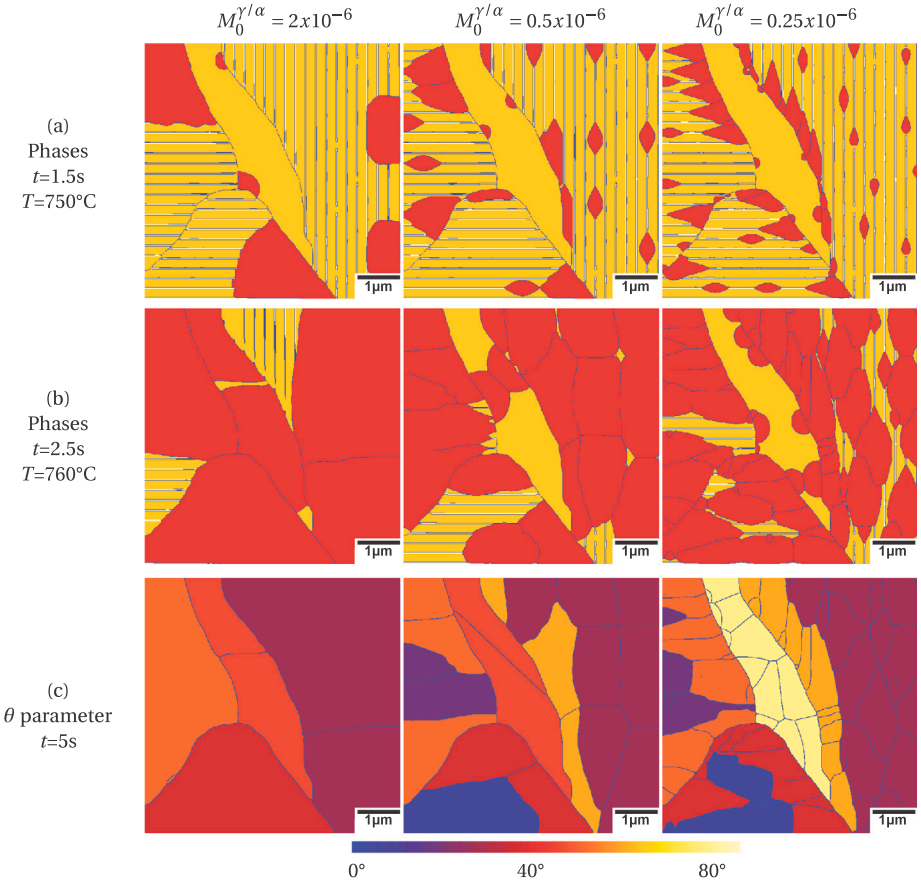

Fig. 12. (a,b) Simulated microstructural evolution at t = 1.5 s and 2.5 s for different γ/α pre-exponential factors ($M_0^{\gamma/\alpha}$) with red grains representing the austenite phase. (c)θ parameter for t = 5 s (fully transformed microstructure) for different $M_0^{\gamma/\alpha}$ ($m^4J^{-1}s^{-1}$), with colors indicating the θ parameter (see Section 4.2).

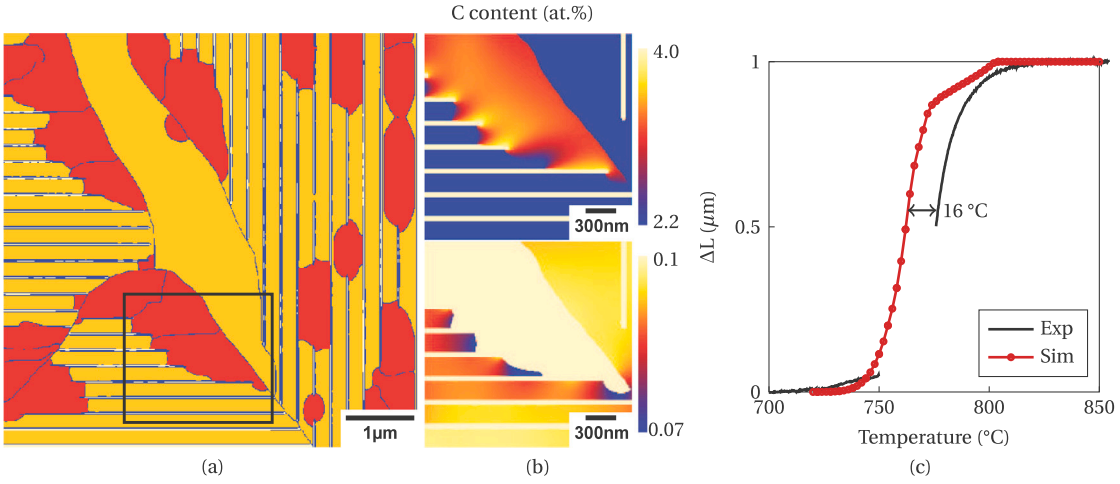

Fig. 13. (a) Phase evolution and (b) carbon content in austenite (top) and ferrite (bottom) of a selected area (black square) for simulation considering 200 °C s^{-1} at t = 0.19 s (758 °C). (c) Austenite fraction as a function of temperature obtained experimentally and via simulation at a heating rate of 200 °C s^{-1}.

°C s^{-1} which is the same order of magnitude as the difference observed between the simulated and experimental curves (16 °C).

A stronger carbon concentration gradient is observed both in austenite and ferrite (Fig. 13a) than obtained for simulations with lower heating rate (Fig. 8a). This is caused by the shorter time for carbon diffusion in the microstructure due to the very high heating rate. As previously mentioned, carbon concentration gradients influence the movement of the γ/α and γ/θ interfaces as regions with high carbon content account for an additional driving force for interface movement. These carbon content inhomogeneities can lead to the formation of different microstructures during cooling. For example, the martensite start temperature is related to the carbon content in the parent austenite which means that martensitic transformation can occur at different temperatures during cooling. Moreover, if the local carbon content leads to the martensite start temperature being below room temperature, then austenite will be stable at room temperature after cooling, characterizing the so-called retained austenite in these regions. Furthermore, the carbon content determines the strength of

the martensite. These effects become even more important if several partial austenitization and quenching steps are considered, such as rails are most likely subjected to in field conditions.

5. Conclusion

The combination of experimental and phase-field simulation analysis of the austenite formation from a pearlitic microstructure was presented in this paper. The results show that:

- Austenite nuclei formed at heating rates of 10 and 200 °C s^{-1} show similar growth morphologies. The main microstructural aspects observed are flat and sharp austenite front, nucleation at colony boundaries and within the colonies, and preferential growth towards a pearlite colony.
- Phase-field simulations of austenite growth from a pearlitic microstructure capture these different morphological features depending on the values of the γ/α and γ/θ interface mobilities. A flat growth front with undissolved cementite is obtained when $M^{\gamma/\theta}$ is lower than $M^{\gamma/\alpha}$ while a sharp front is seen for higher $M^{\gamma/\theta}$ values.
- $M^{\gamma/\alpha}$ has a stronger influence on the kinetics of pearlite to austenite transformation than $M^{\gamma/\theta}$. Lower $M^{\gamma/\alpha}$ reproduces the exact change in kinetics observed at the later stages of pearlite to austenite transformation observed experimentally. At this point the growth of austenite is controlled by the rate of pro-eutectoid ferrite dissolution which is much lower than pearlite due to lack of carbon.
- $M^{\gamma/\theta}$ mainly affects the growth morphology of austenite. This mobility dictates the rate of cementite dissolution and consequently the carbon source for austenite growth.
- Carbon concentration gradients are observed in both austenite and ferrite for simulations with both 10 and 200 °C s^{-1}. This gradient is much stronger for higher heating rates, which is due to the lack of time for carbon to homogenize in austenite. These carbon gradients can lead to inhomogeneities in the microstructure during intercritical heating and cooling such as rails are subjected to in the field.

CRediT authorship contribution statement

V. Mattos Ferreira: Conceptualization, Methodology, Investigation, Writing – original draft, Visualization. **M.G. Mecozzi:** Conceptualization, Investigation, Writing – review & editing. **R.H. Petrov:** Supervision, Writing – review & editing. **J. Sietsma:** Supervision, Writing – review & editing.

Declaration of competing interest

The authors declare the following financial interests/personal relationships which may be considered as potential competing interests: Vitoria Mattos Ferreira reports that financial support was provided by ProRail.

Data availability

Data will be made available on request.

Acknowledgments

This research was carried out under project number S16042a in the framework of the Partnership Program of the Materials innovation institute M2i (www.m2i.nl) and the Technology Foundation TTW (www.stw.nl), which is part of the Netherlands Organization for Scientific Research (www.nwo.nl). We would like to thank ProRail, Netherlands for its financial support and DekraRail for arranging specimens for this research.

References

[1] J.E. Garnham, C.L. Davis, Rail materials, Wheel-Rail Interface Handbook, Woodhead Publishing Limited, 2009, pp. 125–171, http://dx.doi.org/10.1533/9781845696788.1.125.

[2] M. Steenbergen, R. Dollevoet, On the mechanism of squat formation on train rails - Part I: Origination, Int. J. Fatigue 47 (2013) 361–372, http://dx.doi.org/10.1016/j.ijfatigue.2012.04.023.

[3] J.E. Garnham, C.L. Davis, The role of deformed rail microstructure on rolling contact fatigue initiation, Wear 265 (9–10) (2008) 1363–1372, http://dx.doi.org/10.1016/j.wear.2008.02.042.

[4] H.C. Eden, J.E. Garnham, C.L. Davis, Influential microstructural changes on rolling contact fatigue crack initiation in pearlitic rail steels, Mater. Sci. Technol. 21 (2005) 623–629, http://dx.doi.org/10.1179/174328405X43207.

[5] F.J. Franklin, J.E. Garnham, C.L. Davis, D.I. Fletcher, A. Kapoor, The evolution and failure of pearlitic microstructure in rail steel - observations and modelling, Wheel-Rail Interface Handbook, Woodhead Publishing Limited, 2009, pp. 311–348, http://dx.doi.org/10.1533/9781845696788.1.311.

[6] J. Takahashi, Atom probe study on microstructure change in severely deformed pearlitic steels: Application to rail surfaces and drawn wires, IOP Conf. Ser. Mater. Sci. Eng. 219 (1) (2017) http://dx.doi.org/10.1088/1757-899X/219/1/012007.

[7] H.W. Zhang, S. Ohsaki, S. Mitao, M. Ohnuma, K. Hono, Microstructural investigation of white etching layer on pearlite steel rail, Mater. Sci. Eng. A 421 (1–2) (2006) 191–199, http://dx.doi.org/10.1016/j.msea.2006.01.033.

[8] G. Baumann, H.J. Fecht, S. Liebelt, Formation of white-etching layers on rail treads, Wear 191 (1–2) (1996) 133–140, http://dx.doi.org/10.1016/0043-1648(95)06733-7.

[9] W. Lojkowski, M. Djahanbakhsh, G. Bürkle, S. Gierlotka, W. Zielinski, H.J. Fecht, Nanostructure formation on the surface of railway tracks, Mater. Sci. Eng. A 303 (1–2) (2001) 197–208, http://dx.doi.org/10.1016/S0921-5093(00)01947-X, arXiv:arXiv:1011.1669v3.

[10] J. Wu, R.H. Petrov, M. Naeimi, Z. Li, R. Dollevoet, J. Sietsma, Laboratory simulation of martensite formation of white etching layer in rail steel, Int. J. Fatigue 91 (2016) 11–20, http://dx.doi.org/10.1016/j.ijfatigue.2016.05.016.

[11] J. Wu, R. Petrov, S. Kölling, P. Koenraad, L. Malet, S. Godet, J. Sietsma, Micro and Nanoscale Characterization of Complex Multilayer-Structured White Etching Layer in Rails, Metals 8 (10) (2018) 749, http://dx.doi.org/10.3390/met8100749, URL http://www.mdpi.com/2075-4701/8/10/749.

[12] W. Osterle, H. Rooch, A. Pyzalla, L. Wang, Investigation of white etching layers on rails by optical microscopy, electron microscopy, X-ray and synchrotron X-ray diffraction, Mater. Sci. Eng. A 303 (2001) 150–157, http://dx.doi.org/10.3109/03014460903198509.

[13] A. Kumar, G. Agarwal, R. Petrov, S. Goto, J. Sietsma, M. Herbig, Microstructural evolution of white and brown etching layers in pearlitic rail steels, Acta Mater. 171 (2019) 48–64, http://dx.doi.org/10.1016/j.actamat.2019.04.012.

[14] G.R. Speich, V.A. Demarest, R.L. Miller, Formation of Austenite During Intercritical Annealing of Dual-Phase Steels, Metall. Trans. A Phys. Metall. Mater. Sci. 12 A (8) (1981) 1419–1428, http://dx.doi.org/10.1007/bf02643686.

[15] D.V. Shtansky, K. Nakai, Y. Ohmori, Pearlite to austenite transformation in an Fe-2.6Cr-1C alloy, Acta Mater. 47 (9) (1999) 2619–2632, http://dx.doi.org/10.1016/S1359-6454(99)00142-1.

[16] Z.D. Li, G. Miyamoto, Z.G. Yang, T. Furuhara, Nucleation of austenite from pearlitic structure in an Fe-0.6C-1Cr alloy, Scr. Mater. 60 (7) (2009) 485–488, http://dx.doi.org/10.1016/j.scriptamat.2008.11.041.

[17] S. Sharma, T. Nanda, M. Adhikary, T. Venugopalan, B.R. Kumar, A simulation study of pearlite-to-austenite transformation kinetics in rapidly heated hot-rolled low carbon steel, Mater. Des. 107 (2016) 65–73, http://dx.doi.org/10.1016/j.matdes.2016.06.025.

[18] G. Shen, C.W. Zheng, J.F. Gu, D.Z. Li, Micro-scale Cellular Automaton Modeling of Interface Evolution During Reaustenitization from Pearlite Structure in Steels, Acta Metallur. Sin. (English Letters) 31 (7) (2018) 713–722, http://dx.doi.org/10.1007/s40195-018-0706-8.

[19] A. Jacot, M. Rappaz, R.C. Reed, Modelling of reaustenitization from the pearlite structure in steel, Acta Mater. 46 (11) (1998) 3949–3962, http://dx.doi.org/10.1016/S1359-6454(98)00048-2.

[20] M. Militzer, Phase field modelling of phase transformations in steels, in: Phase Transformations in Steels, 2012, pp. 405–432, http://dx.doi.org/10.1533/9780857096111.3.405.

[21] V. Savran, Austenite formation in C-Mn steel (Ph.D. thesis), Delft University of Technology, 2009.

[22] R.G. Thiessen, I.M. Richardson, J. Sietsma, Physically based modelling of phase transformations during welding of low-carbon steel, Mater. Sci. Eng. A 427 (1–2) (2006) 223–231, http://dx.doi.org/10.1016/j.msea.2006.04.076.

[23] J. Rudnizki, B. Böttger, U. Prahl, W. Bleck, Phase-field modeling of austenite formation from a ferrite plus pearlite microstructure during annealing of cold-rolled dual-phase steel, Metall. Mater. Trans. A Phys. Metall. Mater. Sci. 42 (8) (2011) 2516–2525, http://dx.doi.org/10.1007/s11661-011-0626-y.

[24] S. Li, Z.N. Yang, M. Enomoto, Z.G. Yang, Study of partition to non-partition transition of austenite growth along pearlite lamellae in near-eutectoid Fe-C-Mn alloy, Acta Mater. 177 (2019) 198–208, http://dx.doi.org/10.1016/j.actamat.2019.07.038.

[25] J. Wu, Microstructure evolution in pearlitic rail steel due to rail/wheel interaction (Ph.D. thesis), Delft University of Technology, 2018, http://dx.doi.org/10.4233/uuid:c536ca47-8981-4a9e-916f-396bcbca4bc5.

[26] M. Militzer, H. Azizi-Alizamini, Phase field modelling of austenite formation in low carbon steels, Solid State Phenomena 172–174 (2011) 1050–1059, http://dx.doi.org/10.4028/www.scientific.net/SSP.172-174.1050.

[27] J. Andersson, T. Helander, L. Hoglund, P. Shi, B. Sundman, THERMO-CALC & DICTRA, Computational Tools For Materials Science, Calphad Comput. Coupl. Phase Diagrams Thermochem. 26 (2) (2002) 273–312, URL http://linkinghub.elsevier.com/retrieve/pii/S0364591602000378.

[28] V. Mattos Ferreira, M.G. Mecozzi, R. Petrov, J. Sietsma, Microstructure Development of Pearlitic Railway Steels Subjected to Fast Heating, SSRN Electron. J. 221 (2022) 110989, http://dx.doi.org/10.2139/ssrn.4108630.

[29] F.G. Caballero, C. Capdevila, C. García De Andrés, Influence of pearlite morphology and heating rate on the kinetics of continuously heated austenite formation in a eutectoid steel, Metall. Mater. Trans. A Phys. Metall. Mater. Sci. 32 (6) (2001) 1283–1291, http://dx.doi.org/10.1007/s11661-001-0218-3.

[30] A. Roósz, Z. Gácsi, E.G. Fuchs, Isothermal formation of austenite in eutectoid plain carbon steel, Acta Metall. 31 (4) (1983) 509–517, http://dx.doi.org/10.1016/0001-6160(83)90039-1.

[31] I. Steinbach, F. Pezzolla, B. Nestler, M. Seeßelberg, R. Prieler, G.J. Schmitz, J.L. Rezende, A phase field concept for multiphase systems, Physica D 94 (3) (1996) 135–147, http://dx.doi.org/10.1016/0167-2789(95)00298-7.

[32] J. Eiken, A Phase-Field Model for Technical Alloy Solidification (Ph.D. thesis), Rheinisch-Westfälischen Technischen Hochschule Aachen, 2021.

[33] M. Militzer, Phase field modeling of microstructure evolution in steels, Curr. Opin. Solid State Mater. Sci. 15 (3) (2011) 106–115, http://dx.doi.org/10.1016/j.cossms.2010.10.001.

[34] https://micress.rwth-aachen.de/ URL https://micress.rwth-aachen.de/.

[35] G.P. Krielaart, S. Zwaag, Kinetics of gamma to alpha phase transformation in Fe-Mn alloys containing low manganese, Mater. Sci. Technol. 14 (1998) 10–18.

[36] T. Nagano, M. Enomoto, Calculation of the interfacial energies between α and γ iron and equilibrium particle shape, Metall. Mater. Trans. A 37 (12) (2006) 929–937, http://dx.doi.org/10.1007/s11661-006-1013-y.

[37] H. Azizi-Alizamini, M. Militzer, Phase field modelling of austenite formation from ultrafine ferrite-carbide aggregates in Fe-C, Int. J. Mater. Res. 101 (4) (2010) 534–541, http://dx.doi.org/10.3139/146.110307.

[38] M.G. Mecozzi, M. Militzer, J. Sietsma, S. van der Zwaag, The Role of Nucleation Behavior in Phase-Field Simulations of the Austenite to Ferrite Transformation, Metall. Mater. Trans. A 39 (June) (2008) 1237–1247, http://dx.doi.org/10.1007/s11661-008-9517-2.

[39] G.R. Speich, V.A. Demarest, R.L. Miller, Formation of Austenite During Intercritical Annealing of Dual-Phase Steels., Metall. Trans.. A Phys. Metall. Mater. Sci. 12 A (8) (1981) 1419–1428, http://dx.doi.org/10.1007/bf02643686.

[40] M.G. Mecozzi, J. Eiken, M. Apel, J. Sietsma, Quantitative comparison of the phase-transformation kinetics in a sharp-interface and a phase-field model, Comput. Mater. Sci. 50 (6) (2011) 1846–1853, http://dx.doi.org/10.1016/j.commatsci.2011.01.028.

[41] M. Militzer, M.G. Mecozzi, J. Sietsma, S. van der Zwaag, Three-dimensional phase field modelling of the austenite-to-ferrite transformation, Acta Mater. 54 (15) (2006) 3961–3972, http://dx.doi.org/10.1016/j.actamat.2006.04.029.